Journal of
Materials Chemistry A

Accepted Manuscript

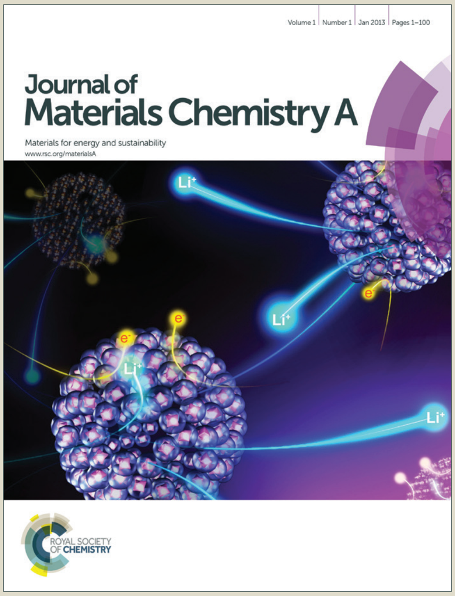

ROYAL SOCIETY
OF CHEMISTRY

www.rsc.org/materialsA

Journal of Materials Chemistry A

Cite this: DOI: 10.1039/c0xx00000x

www.rsc.org/xxxxxx

PAPER

A Novel recyclable dual-heterostructured Fe_3O_4@CeO_2 /M (M= Pt, Pd and Pt-Pd) catalysts: Synergetic and redox effects for superior catalytic performance

Qin Wang[1,2], Yingjun Li, Baocang Liu, Qing Dong, Guangran Xu, Li Zhang and Jun Zhang[1,2]*

[1]College of Chemistry and Chemical Engineering, Inner Mongolia University, Hohhot 010021, P.R. China

[2]Inner Mongolia Key Lab of Nanoscience and Nanotechnology, Hohhot 010021, P.R. China

Received (in XXX, XXX) Xth XXXXXXXXX 20XX, Accepted Xth XXXXXXXXX 20XX
DOI: 10.1039/b000000x

We report the creation of highly efficient dual-heterostructured catalysts consisting of magnetic Fe_3O_4 cores, CeO_2 shells and coated with noble metal nanoparticles (NMNPs) (Pt, Pd and Pt-Pd nanoparticles). These intriguing dual-heterostructural features which are in favor of reactant diffusion and exposure of active sites can enhance synergistic catalytic effects between the NMNPs and CeO_2 nanoparticle. And the synergistic catalytic effect and redox effect features between Fe_3O_4 and CeO_2 are beneficial for superior catalytic and electrochemical performance. Impressively, the resultant Fe_3O_4@CeO_2/Pd (3 wt.%) and Fe_3O_4@CeO_2/Pt (20 wt.%) catalysts manifest superior catalytic efficiency and electrocatalytic reactivity toward the reduction of 4-nitrophenol and oxidation of methanol in alkaline solution, demonstrating the significance of the dual-heterostructural of these recyclable catalysts. This synthetic strategy provides a new methodology for the fabrication of other high-performance and multifunctional catalysts, which would be very useful in various catalytic reactions.

Introduction

With the globalization of economy, phenolic wastewater pollution has become one of the strategic issues.[1-3] To date, the catalytic hydrogenation which can be conducted under a relatively mild condition without the by-products of contaminated disposals is a promising method for phenolic wastewater treatment. Heterostructural catalysts composed of different metals and metal oxides into an integrated structure are a fascinating class of materials that may maintain the properties of each component, as well as manifest higher catalytic performance due to their structure features.[4-8] However, heterostructural catalysts exhibit relatively high reaction rate in the catalytic water treatment, the difficulty of their recycle from treated water may cause their redispersion into the water environment. Therefore, these nanocatalysts are sometimes utilized by complex methods, such as tedious centrifugation and filtration. In this increasingly environmentally conscious age, search for an efficient recoverable catalyst has become inexorable. Magnetic separation could be a more efficient technique to remove these nanocatalysts from water environment. In this regard, integrating magnetic Fe_3O_4 NPs into heterostructural materials as a magnetically recoverable catalyst could be a promising method. Fe_3O_4 NPs have gained much attention due to their rapid response to an applied magnetic field, which are often hybridized with the catalysts to form magnetic nanocatalysts that make it possible to realize convenient recycling of catalysts.[9-15]

Noble metals nanoparticles (NMNPs), especially Pt and Pd have wide range of applications such as catalysis, electrochemical, energy processing, and pollution control.[16-17] To enhance their catalytic activity and stability, lots of oxides have been used as catalyst supports for the deposition of these NMNPs. CeO_2, which has a Ce^{4+}/Ce^{3+} redox cycles is an ideal candidate due to its low cost, high oxygen storage capability and high oxygen mobility.[18-19] However, due to its poor conductivity, it is necessary to modify the CeO_2 nanoparticles to increase its electrochemical conductivity and subsequently the catalytic performance. Loading NMNPs onto cerium oxide can dramatically improve catalytic and electrochemical activities owing to their synergetic catalytic effects between CeO_2 nanoparticles and NMNPs.[20]

Herein, we report a novel dual-heterostructured Fe_3O_4@CeO_2/M (M=Pt, Pd and Pt-Pd) catalysts, which are composed of magnetic Fe_3O_4 cores, porous CeO_2 shells and coated with NMNPs. These dual-heterostructural features which are in favor of reactant diffusion and exposure of active sites can dramatically enhance synergistic catalytic effect between the NMNPs and CeO_2 shells. And the synergistic catalytic and redox effects features between Fe_3O_4 and CeO_2 are beneficial for superior catalytic and electrochemical activities. The catalytic activity of the dual-heterostructural catalysts were systematically tested using the 4-NP reduction and oxidation of methanol in alkaline solution as model reactions. The results indicated that the catalytic efficiency varies with the dual-heterostructure and the kinds of NMNPs. Impressively, the resultant Fe_3O_4@CeO_2/Pd (3%) catalyst exhibits superior catalytic performance toward catalytic reduction of 4-NP to 4-AP. And the Fe_3O_4@CeO_2/Pt (20%) catalyst manifests superior electrochemical activities toward oxidation of methanol in alkaline solution. Our results therefore provide a general approach based on a dual-heterostructural for preparation and discovery of highly efficient and magnetic nanocatalysts, which would be very useful in various catalytic reactions.

Experimental

Synthesis of magnetite microspheres

The magnetite microspheres were prepared according to the following method. Typically, $FeCl_3 \cdot 6H_2O$ (1.35g, 5 mmol), polyethylene glycol (1.0 g) and NaAc (3.6 g) were dissolved in 40 mL of ethylene glycol with stirring for 30 min to form a clear solution. Then the obtained solution was transferred into a 50 mL Teflon-lined stainless steel autoclave. The autoclave was heated at 200 °C for 8 h. The precipitate was collected by centrifuge and then washed with ethanol and deionized water for several times.

Synthesis of ceria precursor

The ceria precursor was prepared by the solvothermal method. 1 g Ce $(NO_3)_3 \cdot 6H_2O$ and 1 g NaOH were separately dissolved in 20 mL of ethanol. The mixture was stirred vigorously for 24 h at 50 °C. Hydrogen peroxide (30 % H_2O_2, 0.05 mL) was taken into the mixture solution, stirred for 2 h. The precipitate was washed and collected by centrifugation before drying at 60 °C for 4 h. 1 g of precipitate was then dispersed in 20 mL distilled water under continuous stirring. Then, the pH of the solution was adjusted to 0.1 by adding concentrated nitric acid. The reaction was allowed to proceed at 40 °C for 2 h under continuous stirring. After the solution was cooled to room temperature naturally, the transparent light yellow solution was obtained.

Synthesis of Fe_3O_4@CeO_2/Pd spheres

The Fe_3O_4@CeO_2 microspheres were prepared in accordance with the following procedure: 0.1 g of Fe_3O_4 nanoparticles was dispersed in a mixture containing 30 mL distilled water and 3 mL of ceria precursor through an ultrasonic treatment process for 15 min. Subsequently, 0.5 mol/L ammonium hydroxide solution was added to adjust the pH to 6.8. The final mixed solution was agitated vigorously by stirring for 4 h at a constant temperature of 60 °C. After the reaction was completed, the particles was collected through an external magnet and washed thoroughly with ethanol before drying at 60 °C overnight. An aqueous solution of $PdCl_2$ (10 mL) and polyvinyl alcohol (PVA, 1 wt. %, 0.72 mL) were diluted by water (120 mL). After stirring for 30 min, 0.1 M $NaBH_4$ (1.98 mL) was added to form a dark brown sol. Subsequently, sulfuric acid solution was added to adjust the pH to 1. Then, 0.2 g of Fe_3O_4@CeO_2 was ultrasonically dispersed in the mixture under vigorous stirring. After 2 h, the resulting slurry was filtered, washed three times with distilled water and absolute alcohol to remove the surface-adsorbed PVA on the surface of the samples, and finally dried in a vacuum oven at 60 °C overnight. Finally, the as-prepared nanoparticles were calcined in N_2 at 300 °C for 2 h.

Synthesis of Fe_3O_4@CeO_2/Pt spheres

Pt nanoparticles were supported on Fe_3O_4@CeO_2 nanocrystals by using the sol-immobilization method. An aqueous solution of $H_2PtCl_6 \cdot 6H_2O$ (16.0 mL) and polyvinyl alcohol (PVA, 1 wt. %, 0.72 mL) were diluted by water (120 mL). After stirring for 30 min, 0.1 M $NaBH_4$ (1.98 mL, $NaBH_4$/Pt=5) was added to form a dark brown sol. Subsequently, sulfuric acid solution was added to adjust the pH to 1. Then, 0.2 g of Fe_3O_4@CeO_2 was ultrasonically dispersed in the mixture under vigorous stirring. After 2 h, the resulting slurry was filtered, washed several times with distilled water and absolute alcohol to remove the surface-adsorbed PVA on the surface of the sample, and finally dried in a vacuum oven at 60 °C overnight. Finally, the resultant samples were calcined in N_2 at 300 °C for 2 h.

Synthesis of Fe_3O_4@CeO_2/Pt-Pd spheres

An aqueous solution of $H_2PtCl_6 \cdot 6H_2O$ (8.0 mL) and $PdCl_2$ (5.0 mL) and polyvinyl alcohol (PVA, 1 wt. %, 0.72 mL) were diluted by water (120 mL). After stirring for 30 min, 0.1 M $NaBH_4$ (1.98 mL, $NaBH_4$/Pt=5) was added to form a dark brown sol. Subsequently, sulfuric acid solution was added to adjust the pH to 1. Then, 0.2 g of Fe_3O_4@CeO_2 was ultrasonically dispersed in the mixture under vigorous stirring. After 2 h, the resulting slurry was filtered, washed several times with distilled water and absolute alcohol to remove the surface-adsorbed PVA on the surface of the sample, and finally dried in a vacuum oven at 60 °C overnight. Finally, the resultant samples were calcined in in N_2 at 300 °C for 2 h.

Characterization

Transmission electron microscopy (TEM) characterization was performed on a JEM-2010 system and a HITACHI 800 system operated at acceleration voltages of 120 kV and 200 kV, respectively. Powder X-ray diffraction (XRD) measurements were performed using a PuXi XD3 diffractometer (Cu Kα radiation, $\lambda = 0.15406$ nm). Magnetic measurements were carried out using a vibrating sample magnetometer (VSM; Digital Measurement System JDM-13). X-ray photoelectron spectroscopy (XPS) measurements were performed in a VG Scientific ESCALAB Mark II spectrometer equipped with two ultrahigh-vacuum (UHV) chambers. Surface area measurements were performed on an ASAP 2010 Brunauer-Emmett-Teller (BET) analyzer. The absorption spectra were recorded using a SPECORD.50 UV-vis spectrophotometer (Analytikjena). Actual metal content in the catalysts were estimated with a ICP-Mass spectroscopy (VARIAN VISTA-MPX).

Catalytic tests

The catalytic performance of the catalysts was tested by employing the reduction of 4-nitrophenol to 4-aminophenol as a model reaction. Typically, the catalyst (2 mg) was added to deionized water (40 mL) to form a homogeneous suspension by ultrasonication. Then, $NaBH_4$ aqueous solution (0.5 M, 0.5 mL) was added to the above suspension, and the suspension was stirred at room temperature for 10 min. Then, 4-nitrophenol (0.012 M, 0.25 mL) was infused into the above suspension. After stirring several seconds, the mixture was rapidly transferred to the quartz cell to monitor the reaction progress by measuring the UV-vis absorption spectra of the mixture to evaluate the catalytic activity and stability of the catalysts.

Preparation of catalysts modified GCE

Before the modification, a GCE (3.0 mm in diameter) was polished with 0.05 μm α-Al_2O_3 powder, and then ultrasonically rinsed by ethanol and ultrapure water, dried in N_2 at room temperature. To prepare a catalyst-coated working electrode, the catalyst was dispersed in a mixture of solvents containing water, ethanol and Nafion® (5%) (v / v / v = 15/5/1) and form a 10 mg mL^{-1} suspension. And 0.01 mL catalyst ink was then dropped onto the GCE surface and dried at room temperature to finish the modification. Commercial Pt/C (10% Pt) catalyst was prepared the same way and used for contrast experiment.

Electrochemical measurements

Voltammetric measurements were carried out with a CHI 750D electrochemical workstation. Ag/AgCl and Pt wire were used as the reference electrode and counter electrode, respectively. The electrodes were immersed in the nitrogen saturated 0.5 M H_2SO_4 solution (25 °C), and the potential was scanned from -0.2 to 0.3 V at a scan rate of 50 mV s^{-1}. The scan was repeated several times to ensure that a stable cyclic voltammogram (CV) was obtained. The CVs were used to estimate the electrochemically active surface area (EASA) of the catalyst by calculating the hydrogen under potential desorption (Hupd) area of the catalyst. CVs for MOR were conducted in 0.5M KOH and 1.0 M methanol from -0.9 V to 0.5 V at a scan rate of 50 mV s^{-1}. The amperometric current density–time (i–t) curves were measured at a fixed potential for 3600 s in 0.5 M KOH and 1.0 M CH_3OH. For each catalyst, the current was normalized to the loading of noble metals (Pt) to obtain mass activity. All experiments were conducted at room temperature.

Results and Discussion

The synthesis procedures of $Fe_3O_4@CeO_2/M$ heterostructural nanocatalysts involve several steps (Scheme 1). As illustrated in Scheme 1, the synthesis of these microspheres involves three steps, and each step is well controlled. After coating, the NMNPs were uniformly distributed on the surface of the oxide microspheres.

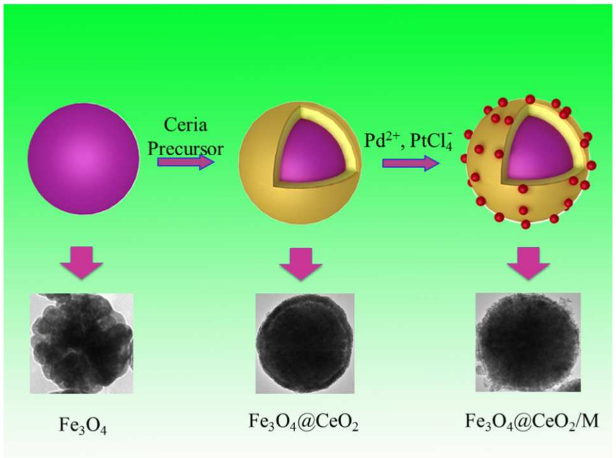

Scheme.1 Schematic illustration of the preparation procedures of the heterostructural microspheres and their corresponding TEM images.

The crystal structures of the as-synthesized nanocatalysts were examined using X-ray diffraction (XRD). Fig.S1 shows the XRD patterns of typical nanocatalysts. The diffraction peaks corresponding to the lattice planes of (111), (220) (2θ=47.5°) and (311) (2θ=57°) are clearly discerned and can be readily indexed to the pure cubic fluorite structure of CeO_2 with a lattice constant of a=5.410 Å, a value very close to the reported data (JCPDS No.34-0394, a=5.411 Å).[21] And the (220) (2θ=30°), (311) (2θ=35.4°), (400), (511), and (440) planes can be indexed to the face-centered cubic phase of Fe_3O_4 with a lattice constant of a =8.392 Å, which is very close to the reported data (JCPDS No. 85-1436, a=8.393 Å).[22] The positions and their relative intensities of the reflection peaks agree well with those of CeO_2 and Fe_3O_4 nanocrystals reported in the literature. No noble metals signals are detected due to low actual content loading on the surface of the $Fe_3O_4@CeO_2$ supports (Actual content of Pt and Pd are 1.36 wt. % and 1.62 wt. %, respectively).

The morphologies and the sizes of the $Fe_3O_4@CeO_2/M$ (M=Pt, Pd and Pt-Pd) catalysts are shown in Fig.1. It reveals that the obtained $Fe_3O_4@CeO_2/M$ catalysts with sizes in the range of 300-350 nm, and CeO_2 nanospheres are composed of a large of tiny nanoclusters that are assembled *in situ* to form the nanocrystals. The NMNPs, with average diameter of about 3 nm, are well-dispersed on the surface of the CeO_2 nanocrystals, and no obvious aggregation is observed. The HAADF-STEM and elemental mapping have also been performed to reveal the element distribution in the heterostructures microspheres. It reveals that the NMNPs observed as white dots are remarkably well-dispersed on the surface of $Fe_3O_4@CeO_2$ microspheres (Fig.2). The mapping results (Fig.2e-2l) indicate that the elements Fe, Ce, O, Pt and Pd spread evenly in the whole spheres and the Ce and NMNPs are almost located on the outermost surface of the microspheres, which confirms the dual-heterostructure of $Fe_3O_4@CeO_2/M$ as obtained by the step-by-step assembly procedures illustrated in Scheme1.

X-ray photoelectron spectra (XPS) was also employed to examine the surface elements and their valence states (Fig 3). The XPS elemental survey scan of the surface of the Pd-loaded $Fe_3O_4@CeO_2$ microspheres reveals that oxygen, cerium, carbon and palladium are present in the samples, as show in Fig 3a. Regarding the typical signals of Ce3d spectra, the four main $3d_{3/2}$ peaks features at around 917.4 eV, 908.5 eV, 905.2 eV and 901.7 eV correspond to the α_1, α_2, α_3 and α_4 components, while the $Ce3d_{5/2}$ located at 898.8 eV, 889.9 eV, 887.3 eV, and 883.1 eV correspond to β_1, β_2, β_3, and β_4, respectively (Fig.3b). The signals α_3 and β_3, characteristics of Ce^{3+}, exist in the $Fe_3O_4@CeO_2/Pd$ catalyst, while other peaks are corresponding to the Ce^{4+}. The presence of Ce^{3+} is contributed to the interaction between ceria and the surrounding palladium and oxygen atoms which may lead to a transfer of the lattice oxygen in CeO_2 lattice. In Fig 3c, the regional XPS spectrum of $Fe_3O_4@CeO_2/Pd$ exhibits two peaks centered at 341.1 and 335.7 eV, which are assigned to Pd (0) of $3d_{3/2}$, and $3d_{5/2}$, respectively. The regional XPS spectrum of Pd indicates that the Pd (0) species are formed on the surface of $Fe_3O_4@CeO_2$ microspheres. The spectra for the O1s ionization feature were fitted with Gaussian-Lorenz features as shown in Fig. 3d. The primary peak located at around 532.3 eV denoted as adsorption oxygen (O_{ads}) is ascribed to the chemisorbed oxygen caused by the adsorption of H_2O and CO_2 molecule to the surface. And the additional peak features at 530.3eV denoted as lattice oxygen (O_{lat}) is mainly ascribed to the Fe_3O_4 and ceria support.

Journal of Materials Chemistry A

Dynamic Article Links ▶

Cite this: DOI: 10.1039/c0xx00000x

www.rsc.org/xxxxxx

PAPER

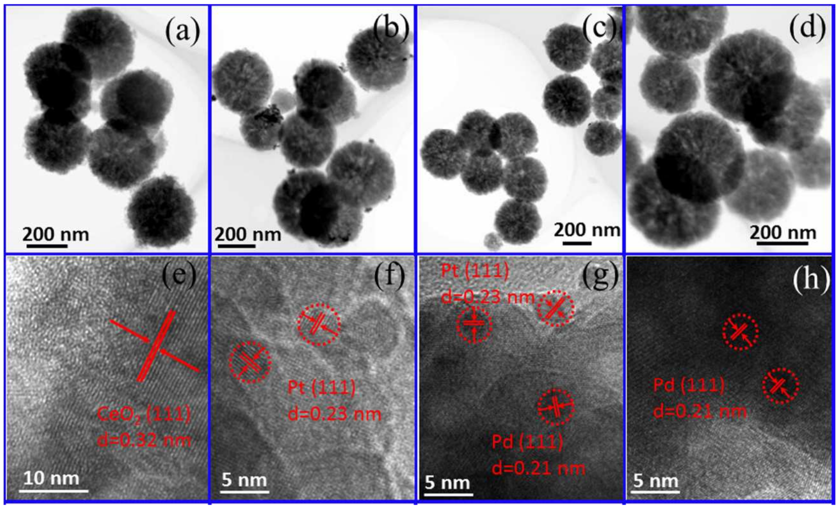

Fig. 1 TEM and HR-TEM images of Fe_3O_4@CeO_2 (a) (e); Fe_3O_4@CeO_2/Pt (3wt.%) (b) (f); Fe_3O_4@CeO_2/Pt-Pd (3wt.%) (c) (g) and Fe_3O_4@CeO_2/Pd (3wt.%) catalysts (d) (h).

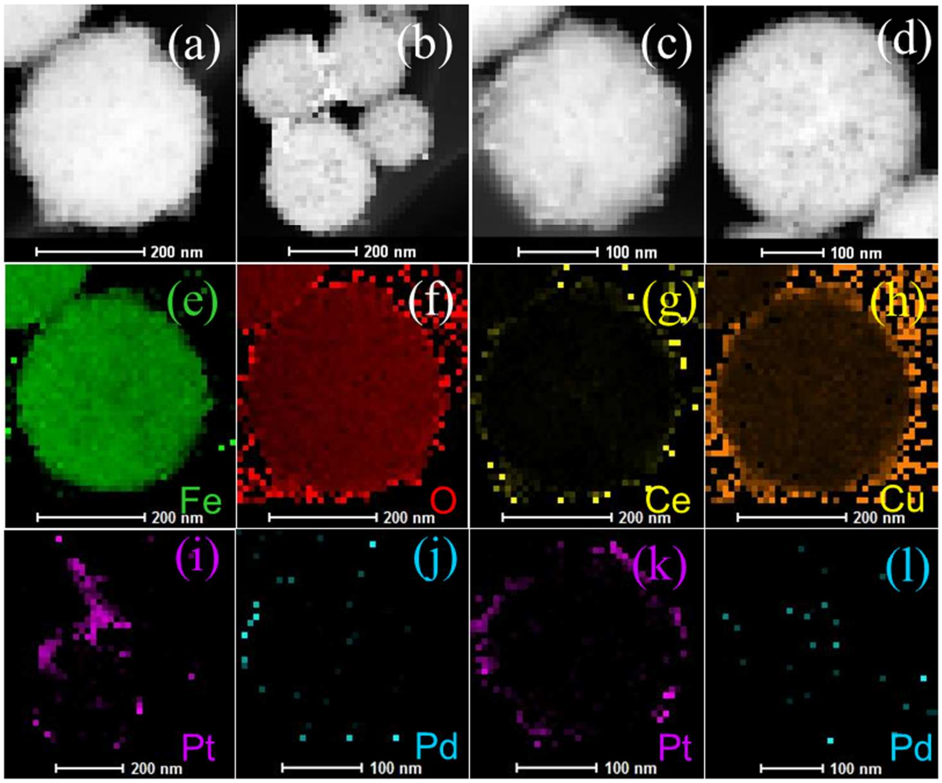

Fig. 2 HAADF-STEM images of (a) Fe_3O_4@CeO_2, (b) Fe_3O_4@CeO_2/Pt (3wt.%), (c) Fe_3O_4@CeO_2/Pd-Pt (3wt.%) and (d) Fe_3O_4@CeO_2/Pd (3wt.%), and mapping results of the elements (e) Fe, (f) O, (g) Ce, (h) Cu of the Fe_3O_4@CeO_2, (i) Pt, (j) Pd, (k) Pt and (l) Pd corresponding to Fe_3O_4@CeO_2/Pt (3wt.%) (i), Fe_3O_4@CeO_2/Pd-Pt (3wt.%) (j and k) and Fe_3O_4@CeO_2/Pd (3wt.%) (l), respectively.

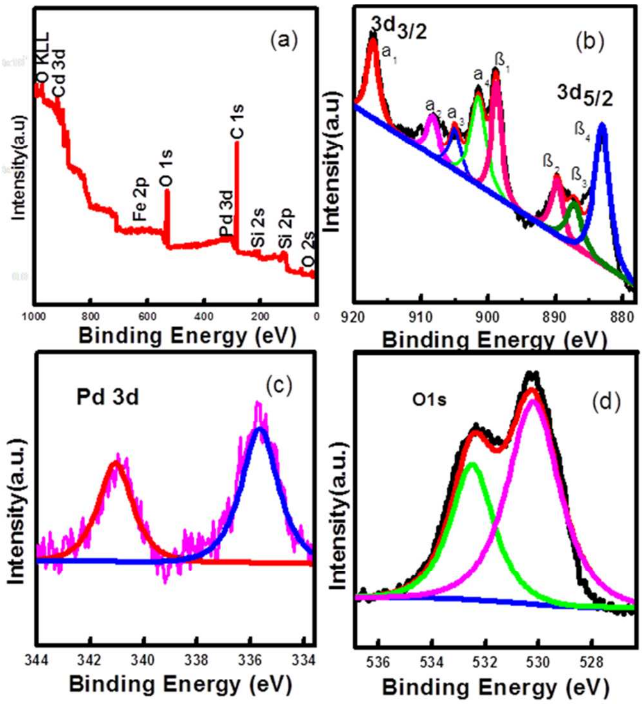

Fig. 3 Experimental and fixed XPS spectra of the Fe_3O_4@CeO_2/Pd catalyst: (a) full spectrum, (b) Ce3d, (c) Pd3d and (d) O1s.

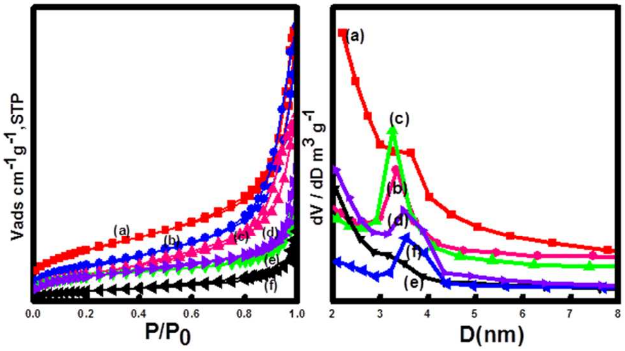

Fig.4 N_2 adsorption-desorption isotherms and BJH measurements of (a) CeO_2, (b) Fe_3O_4@CeO_2, (c) Fe_3O_4@CeO_2/Pd, (d) Fe_3O_4@CeO_2/ Pt-Pd, (e) Fe_3O_4@CeO_2/Pt, (f) Fe_3O_4.

The mesoporous structure was evaluated by the measurement of N_2 adsorption-desorption isotherms and the Brunauer-Emmett-Teller (BET) surface areas (Fig.4). The results indicate that the adsorption-desorption isotherm of the Fe_3O_4@CeO_2/M catalysts has a type IV-like with an apparent H3 hysteresis loop at relatively higher P/P_0, indicating the presence of mesoporous structure. The BET surface areas of the Fe_3O_4@CeO_2/Pd, Fe_3O_4@CeO_2/Pt and Fe_3O_4@CeO_2/Pd-Pt catalysts are 96.2 $m^2 g^{-1}$, 81.6 $m^2 g^{-1}$ and 84.7 $m^2 g^{-1}$, respectively.

The magnetic properties of the nanocatalysts were investigated via a vibrating sample magnetometer (VSM) at room temperature. Fig.5 shows the presence of hysteresis loops, revealing a strong magnetism with negligible coercivity and remanence magnetization at room temperature. For Fe_3O_4, Fe_3O_4@CeO_2 and Fe_3O_4@CeO_2/Pd microspheres, the saturation magnetization (*Ms*) values are 74.7, 31.3 and 34.2 emu.g^{-1}, respectively. The differences in *Ms* are attributed to the existence of CeO_2 and Pd nanoparticles, dual-heterostructure and magnetocrystalline anisotropy. Thus, the Fe_3O_4@CeO_2/M can easily disperse in the absence of a magnetic field, and can be rapidly separated from the mixture within 10 s with the help of the magnet (inset in Fig. 5). This excellent magnetic response behavior of Fe_3O_4@CeO_2/M microspheres contribute to rapid and high throughput enrichment and separation.

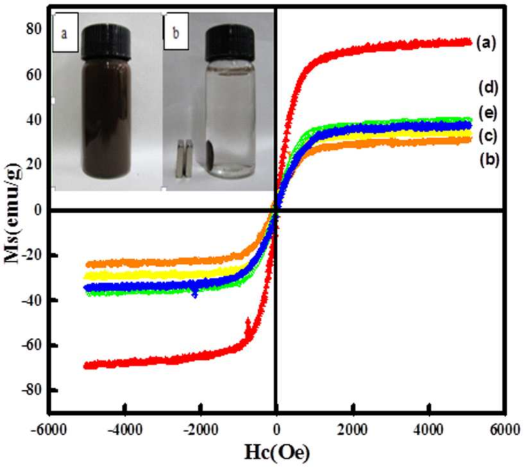

Fig.5 Magnetization curves of the samples measured at 298K: (a) Fe_3O_4, (b) Fe_3O_4@CeO_2, (c) Fe_3O_4@CeO_2/Pd, (d) Fe_3O_4@CeO_2/Pt, (e) Fe_3O_4@CeO_2/Pd-Pt. Photographs (inset) of the samples dispersed in aqueous solution without and with an external magnetic field.

The reduction of 4-NP to 4-AP by $NaBH_4$ over various nanocatalysts was used as a model reaction to evaluate the catalytic activity, and further to study the relationship between the different hybrid structures and their catalytic hydrogenation performance. The evolution process with reaction time for the reduction of 4-NP to 4-AP over different catalysts is monitored by UV-vis spectra (Fig.6). In a typical catalytic reaction, upon the addition the $NaBH_4$, the absorption peak of 4-NP undergoes a red shift from 317 nm to 400 nm due to the formation of 4-nitrophenolate (Fig.6a). After adding 1 mg of catalyst into the system, the reduction of 4-NP was started, the absorption peak at 400 nm gradually decreased in intensity along with the increase of a new absorption peak at about 317 nm, indicating the formation of 4-AP. The results of reduction reaction over Fe_3O_4@CeO_2/Pd (3 wt.%) catalyst indicate that the CeO_2-Pd catalytic system exhibit superior catalytic activity and the 4-NP can be completely reduced into 4-AP within 3 min. The catalytic performance of the Fe_3O_4@CeO_2/Pd catalyst is superior to that of Fe_3O_4@CeO_2/Pt and Fe_3O_4@CeO_2/Pt-Pd catalysts. This result indicates that loading Pd nanoparticles onto Fe_3O_4@CeO_2 nanoparticles can dramatically improve the catalytic activity. And the superior catalytic activity of Fe_3O_4@CeO_2/Pd catalyst is mainly due to their unique dual-heterostructures. First, the mesoporous CeO_2 shells coated onto the surface of the magnetite favor the fast diffusion of reactants and the more active sites exposure, which are beneficial for heterogeneous catalysis. Second, the hierarchical structure and synergistic effect between the NMNPs and the CeO_2 shells will speed up the rate of charge transfer and effectively accelerate the reduction of 4-NP to 4-AP. Third, a competitive redox reaction between CeO_2 and Fe_3O_4 nanoparticles in BH_4^- systems, which is thermodynamically favored can also speed up the rate of charge transfer. And finally, the CeO_2 shells can restrict the NMNPs from growing larger during the synthesis and expose more active sites, thus improving the catalytic efficiency.[23-24] The possible schematic diagram of the reaction mechanism is shown in Scheme 2. The catalytic performance towards the reduction of 4-nitrophenol over Fe_3O_4@CeO_2/Pd and Fe_3O_4@CeO_2/Pt catalysts are both higher than others samples, suggesting the existence of synergistic catalytic effect between the Pd or Pt NPs and the CeO_2 shells. The catalytic stability tests of Fe_3O_4@CeO_2/Pd, Fe_3O_4@CeO_2/Pt microspheres are shown in Fig 6e and Fig 6f. The Fe_3O_4@CeO_2/Pd catalyst exhibits relatively stable catalytic performance even after reaction running for more than twenty cycles. And the catalytic activity of Fe_3O_4@CeO_2/Pt decreased by 20 % after reaction running for more than ten cycles. Because the structural features of CeO_2 shells encapsulation, thin mesoporous shells on Fe_3O_4@CeO_2/M microspheres are in favor of reactant diffusion and exposure of active sites, leading to the improvement of catalytic activity and stability. Noticeably, the Fe_3O_4@CeO_2/Pd catalyst exhibits stable catalytic performance even after running for more than twenty cycles. This may be due to that there exist competitive redox reactions between CeO_2 and Fe_3O_4 nanoparticles in BH_4^- systems. The standard redox potential of Ce^{4+}/Ce^{3+} is 1.44 V, while that of Fe^{3+}/Fe^{2+} is 0.77 V; hence, the transfer of electrons from Fe^{2+} to Ce^{4+} is thermodynamically favored. Cerium (4+) is capable of redox cycling in the presence of BH_4^- and produces Fe^{2+}, behaving similarly to iron in Fenton-like reaction. The redox reactions are as follows:

$$Fe^{3+}+BH_4^- \rightarrow Fe^{2+} \quad (1)$$

$$Fe^{2+}+Ce^{4+} \rightarrow Fe^{3+}+Ce^{3+} \quad (2)$$

$$Fe^{3+}+BH_4^- \rightarrow Fe^{2+} \quad (3)$$

$$Fe^{2+}+Ce^{4+} \rightarrow Fe^{3+}+Ce^{3+} \quad (4)$$

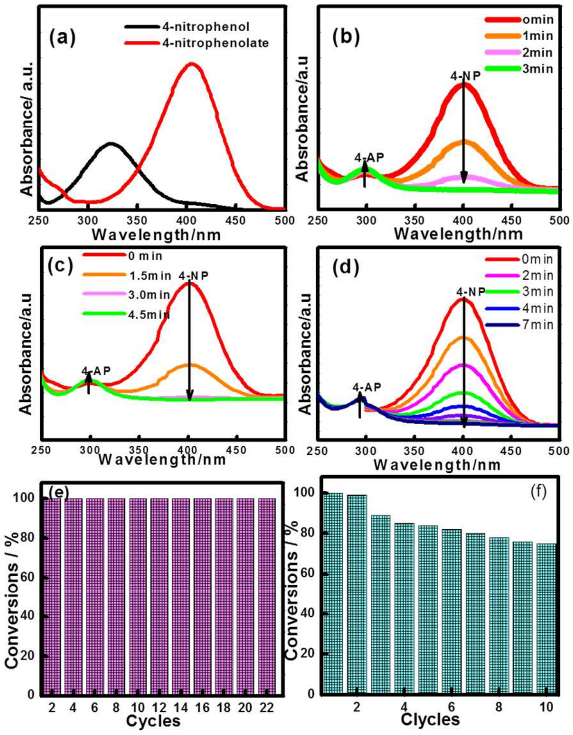

Fig.6 UV-vis spectra of 4-nitrophenol before and after adding $NaBH_4$ solution (a), and the successive reduction of 4-NP to 4-AP over various catalysts: (b) Fe_3O_4@CeO_2/Pd (3 wt.%), (c) Fe_3O_4@CeO_2/Pt (3 wt.%), (d) Fe_3O_4@CeO_2/Pd-Pt (3 wt.%);The catalytic stability tests over: (e) Fe_3O_4@CeO_2/Pd and (f) Fe_3O_4@CeO_2/Pt catalysts.

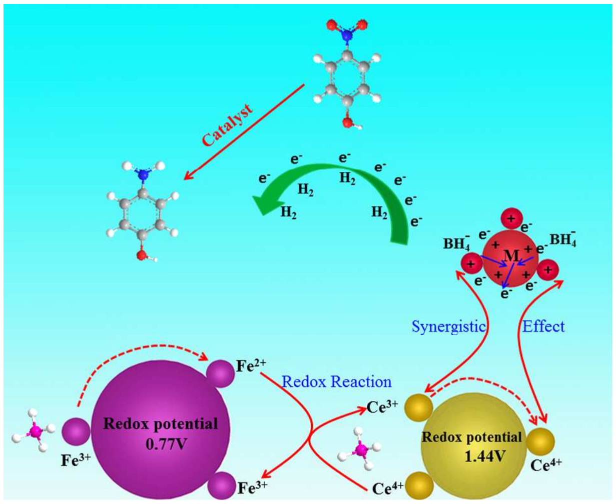

Scheme.2 Schematic diagram of the reaction mechanism of the Fe_3O_4@CeO_2/M catalysts.

Journal of Materials Chemistry A

Dynamic Article Links ►

Cite this: DOI: 10.1039/c0xx00000x

www.rsc.org/xxxxxx

PAPER

Since the amount of $NaBH_4$ greatly exceeded, the reduction are assumed to be a pseudo-first-order to 4-NP concentration. Therefore, the reaction kinetics can be described as followings:

$$\ln (C_t/C_0) = -kt$$

where k is the apparent first-order rate constant (min^{-1}), t is the reaction time. C_t and C_0 are the concentrations of the 4-NP at time t and 0, respectively. As seen from the Fig.S2, the plots all show straight line, indicating the good coincidence with the pseudo-first-order equation. On the basis of the plots, the reaction rate constant per unit mass k for Fe_3O_4@CeO_2/Pd (3 wt.%) were calculated to be 1.29 min^{-1}, suggesting that the Fe_3O_4@CeO_2/Pd catalyst possess higher catalytic activity and efficiency. The actual Pd and Pt contents loaded in various catalysts and their corresponding values of specific surface area (S_{BET}), saturation magnetization (Ms) and the reaction rate constant catalyzed reduction of 4-nitrophenol are shown in Table S1.

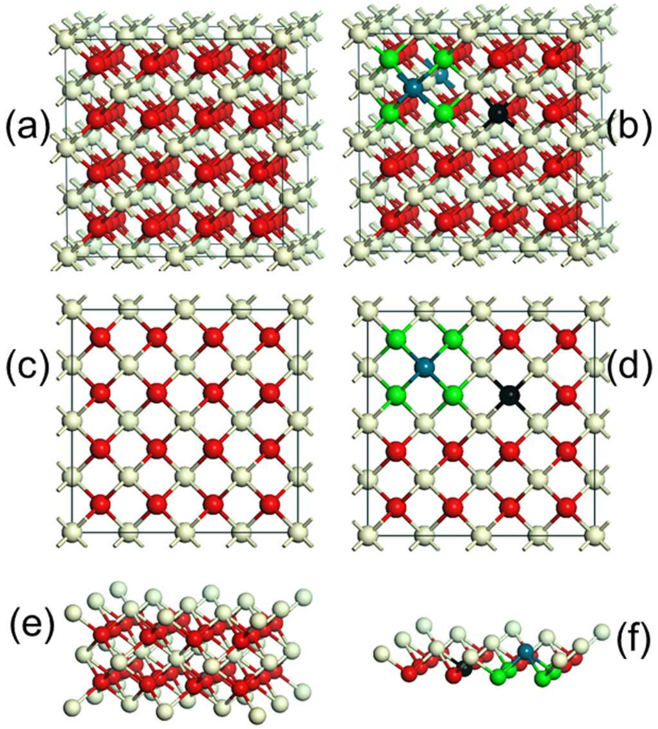

Fig.7 (a) (c) schematic diagram of the CeO_2 cubic crystal lattice. (b)(d) Pd dopant onto CeO_2 surface sitting in a square planar coordination between four lattice oxygen. (e) Side view of the equilibrium surface Ce-O structure. (f) Side view of the equilibrium surface Pd-O-Ce structure. Blue spheres denote the Pd ions, grey and red spheres denote the Ce and O ions respectively. The black spheres represent the position of the charge-compensating vacancy, and the green spheres represent the lattice oxygen.

CeO_2 is a wide band gap insulator that adopts a cubic fluorite structure with a lattice parameter, a, of 5.41 Å (Fig. 7a and 7c). The introduction of Pd^{2+} ions onto CeO_2 surface requires the formation of an equivalent number of O vacancies. The Pd atom substituting for a Ce atom in a C_{2v} symmetric surface site, with subsequent charge-compensating vacancy formation, similar to the calculations of Hermansson and co-works.[25-26] Fig.7b and 7d clearly show that the lattice distortion force existed in CeO_2 crystal lattices maybe place the Pd ions in a square planar coordination environment between four lattice oxygen. And the Pd-O-Ce super-bonds are formed due to the chemical adsorption interaction between the adsorption oxygen and Pd and Ce ions.[27] The surface side views (Fig.7e and 7f) clearly show that the tendency of Pd^{2+} to form square-planar complexes underpins the stability of the active Pd-O-Ce surface superstructure. Despite the reported improvements in CeO_2-Pd catalytic activity, the underlying reasons for superior catalytic performance of Fe_3O_4 @CeO_2/Pd catalyst are in progress.

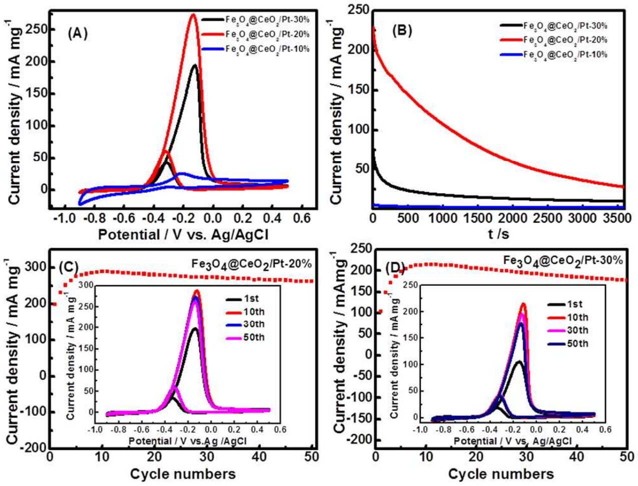

Fig.8 (A) CVs of Fe_3O_4@CeO_2/Pt-10wt.%, Fe_3O_4@CeO_2/Pt-20wt.%, Fe_3O_4@CeO_2/Pt-30wt.% in N_2 saturated 0.5 M KOH and 1.0 M methanol (scan rate: 50 mV s^{-1}); (B) Chronoamperometric (CA) results of methanol oxidation of the Fe_3O_4@CeO_2/Pt-10wt.% catalysts in 0.5 M KOH and 1.0 M methanol at constant voltage of -0.20 V for 1 h. CA curves of Fe_3O_4@CeO_2/Pt-20wt.% and Fe_3O_4@CeO_2/Pt-30wt.% were recorded at -0.12 V; The plots of the forward peak current densities with the number cycles in 0.5 M KOH and 1.0 M methanol over the (C) Fe_3O_4@CeO_2/Pt (20wt.%) and (D) Fe_3O_4@CeO_2/Pt (30 wt.%) catalysts modified electrodes, respectively. Insets (C and D) are the corresponding 1st, 10th, 30th and 50th cyclic voltammograms at a scan rate of 50 mVs^{-1}.

Cyclic voltammetry (CV) and chronoamperometric (CA) were used to evaluate the comparative electrochemical properties of these heterostructure nanocatalysts in alkaline solution. The electrochemical activity was evaluated and normalized to the real surface area per mass Pt. Fig.8 are the CVs and CA results of the Fe_3O_4@CeO_2/Pt (10-30wt.%) catalysts. It reveals that the methanol current density (j_p^{mass}) of Fe_3O_4@CeO_2/Pt (20 wt.%) catalyst (273.0 mA mg^{-1}) is higher than that of Fe_3O_4@CeO_2/Pt (10 wt.%) (26.3 mA mg^{-1}) and Fe_3O_4@CeO_2/Pt (30 wt.%) (196.4 mA mg^{-1}). This indicates that the electrocatalytic activity of Fe_3O_4@CeO_2/Pt (20 wt.%) is obviously higher than that of other catalysts. The higher methanol oxidation current density over

$Fe_3O_4@CeO_2/Pt$ nanocatalysts were further confirmed by the CA measurements performed in 0.5 M KOH and 1.0 M methanol for 1 hour (Fig. 8B). We can observe that the current intensity decay of the $Fe_3O_4@CeO_2/Pt$ (20 wt.%) is much lower than those of the $Fe_3O_4@CeO_2/Pt$ (10 wt.%) and $Fe_3O_4@CeO_2/Pt$ (30 wt.%) during the entire time range. It reveals that after loading Pt nanoparticles onto the $Fe_3O_4@CeO_2$ surface, the electrical conductivity of catalysts can be significantly improved due to the good electrical conductivity of Pt and strong synergism interactions between CeO_2 and Pt nanoparticles.[28-30] And this can be proved by the HR-TEM and XPS results of these catalysts. Fig.S5 are the HAADF-STEM images of the $Fe_3O_4@CeO_2/Pt$ (10-30wt.%) catalysts and their corresponding mapping results of Pt nanoparticles. Noticeably, it can be seen from FigS5(b) and S5(e) that the Pt NMNPs observed as bright dots are remarkably well-dispersed on the surface of $Fe_3O_4@CeO_2$ microspheres over the $Fe_3O_4@CeO_2/Pt$ (20 wt.%) catalysts. The synergism interactions between CeO_2 and Pt nanoparticles became weaker because of the obvious aggregation on the surface of $Fe_3O_4@CeO_2$ microspheres over the $Fe_3O_4@CeO_2/Pt$ (30wt.%) catalyst. Therefore, the electrocatalytic performance of $Fe_3O_4@CeO_2/Pt$ (20wt.%) is better than the $Fe_3O_4@CeO_2/Pt$ (30 wt.%) catalyst. Fig.S6 is the experimental and fixed XPS spectra of the $Fe_3O_4@CeO_2/Pt$ (10-30 wt.%) catalysts ($Pt4f_{7/2}$). The XPS spectra show that the $Pt4f_{7/2}$ peaks of $Fe_3O_4@CeO_2/Pt$ (30 wt.%) are located at 72.1 eV,which are higher compared with 71.9 eV for $Fe_3O_4@CeO_2/Pt$ (20 wt.%). A different degree of upshift of the peaks position of Pt is observed, which can be attributed to the change of the electronic structure of Pt nanoparticles (Fig.S6).[31] Furthermore, the ratio of the forward oxidation current density to the backward current density (I_f/I_b) are 5.40, 4.50 and 4.60 correspond to the $Fe_3O_4@CeO_2/Pt$ (10wt.%), $Fe_3O_4@CeO_2$ /Pt (20wt.%) and $Fe_3O_4@$ CeO_2/Pt (30wt.%) catalyst, which are higher than the Pt-Pd nanodendrites (3.5), Pt/C (4.60) and Pt black (4.50) catalysts.[32] These results indicate that the $Fe_3O_4@CeO_2/Pt$ catalysts system manifest superior anti-poisoning abilities. Actual Pt contents loaded in various catalysts for methanol electro-oxidation and their corresponding CV parameters (peak potential: E_p, mass-normalized current densities: j_p^{geom} and j_p^{mass}, electrochemically active surface area: EASA, and the ratio of the forward oxidation current density to the backward current density: I_f/I_b) are shown in Table 1.

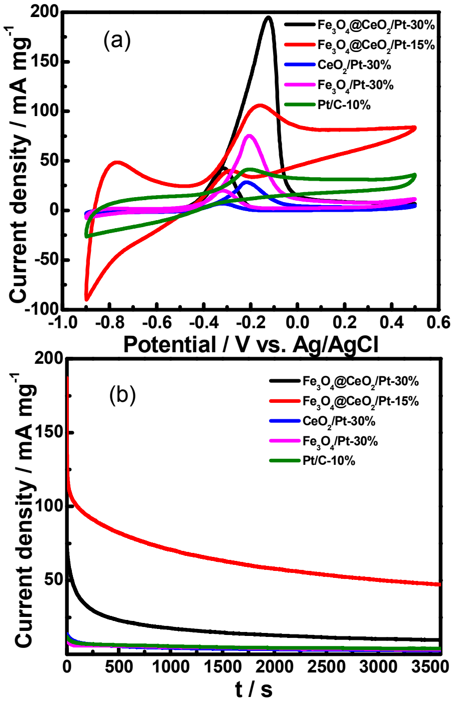

Fig.9 (a) CVs of $Fe_3O_4@CeO_2/Pt$ (30 wt.%), $Fe_3O_4@CeO_2/Pt$ (15 wt.%), Fe_3O_4/Pt (30 wt.%), CeO_2/Pt (30 wt.%) and commercial Pt/C (10 wt.%) in N_2 saturated 0.5 M KOH and 1.0 M methanol (scan rate: 50 mV s^{-1}); (b) CA results of methanol oxidation of the catalysts in 0.5 M KOH and 1.0 M methanol at constant voltage of -0.20 V for 1 h.

Fig.9 shows the CV curves of various catalysts for methanol electro-oxidation in 0.5 M KOH and 1.0 M methanol at the scan rate of 50 mV s^{-1}. The electrochemical activity was evaluated and normalized to the real surface area per mass Pt. It is clear that the methanol current density of $Fe_3O_4@CeO_2/Pt$ (30 wt.%) (196.4 mA mg^{-1}) and $Fe_3O_4@CeO_2/Pt$ (15 wt.%) (105.5 mA mg^{-1}) catalysts are all higher than that of Fe_3O_4/Pt (30 wt.%) (75.3 mA mg^{-1}), CeO_2/Pt (30 wt.%) (29.1 mA mg^{-1}) and commercial Pt/C-10 (wt.%) catalysts (42.4 mA mg^{-1}). This indicates that the electrocatalytic activities of $Fe_3O_4@CeO_2/Pt$ (15-30 wt.%) are obviously higher than that of other catalysts. In addition, the current intensity decay of the $Fe_3O_4@CeO_2/Pt$ (15 wt.%) is much lower than those of the Fe_3O_4/Pt (30 wt.%), CeO_2/Pt (30 wt.%) and commercial Pt/C (30 wt.%) during the entire time range.

Table 1 Actual Pd and Pt contents loaded in various catalysts for methanol electro-oxidation and their corresponding CV parameters (peak potential: E_p, mass-normalized current densities: j_p^{geom} and j_p^{mass}, electrochemically active surface area: EASA, and the ratio of the forward oxidation current density to the backward current density: I_f/I_b)

Samples	Actual Pt content (wt. %)	Ep (V)	EASA (m^2 g^{-1})	j_p^{geom} (mA cm^{-2})	j_p^{mass} (mA mg^{-1})	I_f/I_b
$Fe_3O_4@CeO_2/Pt$-10%	5.0	-0.2	-	0.61	26.3	5.4
$Fe_3O_4@CeO_2/Pt$-20%	16.6	-0.12	61.6	21.6	273.0	4.5
$Fe_3O_4@CeO_2/Pt$-30%	18.3	-0.12	11.4	17.4	196.4	4.6
$Fe_3O_4@CeO_2/Pt$-15%	6.7	-0.15	-	3.5	105.5	2.7
$Fe_3O_4@CeO_2/Pt$-Pd-30%	12.4	-0.2	5.1	4.2	-	4.3
Fe_3O_4/Pt-30%	12.1	-0.2	4.9	4.4	75.3	3.7
CeO_2/Pt-30%	9.0	-0.2	-	1.2	29.1	3.8
Pt/C	10.0	-0.2	-	2.0	42.4	4.6

Journal of Materials Chemistry A

Dynamic Article Links ►

Cite this: DOI: 10.1039/c0xx00000x

www.rsc.org/xxxxxx

PAPER

Conclusions

In summary, a novel dual-heterostructural nanocatalyst with high catalytic efficiency have been fabricated by a self-assembly strategy, which is composed of magnetic Fe_3O_4 cores, mesoporous CeO_2 shells and coated with NMNPs. By rational design of the proper assembled structures, it shows an excellent catalytic performance. These dual-heterostructural features which are in favor of reactant diffusion and active sites exposure can dramatically enhance synergistic catalytic effect between the NMNPs and CeO_2 nanoparticles. The Fe_3O_4@CeO_2 /Pd (3wt.%) nanocatalyst manifest superior catalytic performance than the other catalysts towards the catalytic reduction of 4-NP to 4-AP. And the Fe_3O_4@CeO_2/Pt (20 wt.%) catalyst exhibit superior electrochemical activity towards the oxidation of methanol in alkaline solution. The synthetic strategy may be an effective method for preparation highly efficient dual-heterostructure mesoporous catalysts. And these dual-heterostructures will have great applications not only as catalysts but also in the fields of environmental and biological chemistry.

Acknowledgements

This work was supported by the National Natural Science Foundation of China (NSFC 21201097, NSFC 21467019, NSFC 21261011), Key project of Inner Mongolia National Natural Science Foundation (2010Zd03), Application Program from Inner Mongolia Science and Technology Department (113307), and Program for New Century Excellent Talents in University (NCET-10-0907) and Natural Science Foundation of Inner Mongolia Autonomous Region of china (2014MS0506).

Notes and references

[1] L. Q. Jing, W. Zhou, G. H. Tian and H. G. Fu, *Chem. Soc. Rev.*, 2013, **42**, 9509.

[2] C. D. Wu, X. H. Liu, D. B. Wei, J. C. Fan, and L. S. Wang, *Wat. Res.*, 2001, **35**, 3927.

[3] B. Iurascu, I. Siminiceanu, D. Vione, M. A. Vicente and A. Gil, *Wat. Res.*, 2009, **43**, 1313.

[4] T. Zeng, X. L. Zhang, Y. R. Ma, H. Y. Niu and Y. Q. Cai, *J. Mater. Chem.*, 2012, **22**, 18658.

[5] K. C. Leung, S. H. Xuan, X. M. Zhu, D. W. Wang, C. Chak, S. Lee, W. K. -W. Ho and B. C.-T. Chung, *Chem. Soc. Rev.*, 2012, **41**, 1911.

[6] L. J. Xu and J. L. Wang, *Environ. Sci. Technol.*, 2012, **46**, 10145.

[7] X. Wang, D. P. Liu, S. Y. Song, and H. J. Zhang, *Chem. Eur. J.*, 2013, **19**, 5169.

[8] Q. Wang, W. J. Jia, B. C. Liu, A. Dong, X. Gong, C. Y. Li, P. Jing, Y. J. Li, G. R. Xu and J. Zhang, *J. Mater. Chem. A.*, 2013, **1**, 12732.

[9] R. B. N. Baig and R. S. Varma, *Chem. Commun.,* 2013, **49**, 752.

[10] K. Jiang, H. X. Zhang, Y. Y. Yang, R. Mothes, H. Lang and W. B. Cai, *Chem. Commun.*, 2011, **47**, 11924.

[11] S. K. Li, F. Z. Huang, Y. Wang, Y. H. Shen, L. G. Qiu, A. J. Xie and S. J. Xu, *J. Mater. Chem.*, 2011, **21**, 7459.

[12] H. F. Li, S. Y. Gao, Z. L. Zheng and R. Cao, *Catal. Sci. Technol.*, 2011, **1**, 1194.

[13] Z. J. Wu, C. X. Sun, Y. Chai and M. H. Zhang, *RSC Advances*, 2011, **1**, 1179.

[14] W. Z. Sun, Q. Li, S. A. Gao and J. K. Shang, *J. Mater. Chem. A*, 2013, **1**, 9215.

[15] K. S. Lee, R. M. Anisur, K. W. Kim, W. S. Kim, T. Park, E. J. Kang and I. S. Lee, *Chem. Mater.*, 2012, **24**, 682.

[16] A. J. Amali and R. K. Rana, *Green Chem.*, 2009, **11**, 1781.

[17] C. Lian, H. Q. Liu, C. Xiao, W. Yang, K. Zhang, Y. Liu and Y. Wang, *Chem. Commun.,* 2012, **48**, 3124.

[18] S. Tsunekawa, K. Ishikawa, Z. -Q. Li, Y. Kawazoe and A. Kasuya, *Phys. Rev. Lett.*, 2000, **85**, 3440.

[19] Y. Y. Chu, Z. B. Wang, Z. Z. Jiang, D. M. Gu and G. P. Yin, *Adv. Mater.*, 2011, **23**, 3100.

[20] X. Wang, D. P. Liu, S. Y. Song and H. J. Zhang, *J. Am. Chem. Soc.*, 2013, **135**, 15864.

[21] Q. Wang, W. J. Jia, B. C. Liu, W. Z. Zhao, C. Y. Li, J. Zhang, and G. Xu, *Chem. Asian J.*, 2012, **7**, 2258.

[22] Q. Wang, A. B. Wu, L. X. Yu, Z. L. Liu, W. Xu, and H. Yang, *J. Phys. Chem. C.,* 2009, **113***,* 19875.

[23] B. C. Liu, S. L. Yu, Q. Wang, W. T. Hu, P. Jing, Y. Liu, W. J. Jia, Y. X. Liu, L. X. Liu and J. Zhang, *Chem. Commun.*, 2013, **49**, 3757.

[24] B. C. Liu, Q. Wang, S. L. Yu, T. Zhao, J. X. Han, P. Jing, W. T. Hu, L. X. Liu, J. Zhang, L. D. Sun and C. H. Yan, *Nanoscale.*, 2013, **5**, 9747.

[25] Z. X. Yang, G. X. Luo, Z. S. Lu and K. Hermansson, *J.*

Chem. Phys., 2007,**127**, 074704.

[26] Z. X. Yang, G. X. Luo, Z. S. Lu, T. K. Woo and K. Hermansson, *J. Phys.:Condens. Matter*, 2008, **20**, 035210.

[27] S. Colussi, A. Gayen, M. F. Camellone, M. Boaro, J. Llorca, S. Fabris, and A. Trovarelli, *Angew. Chem*.,2009, **121**, 8633.

[28] Z. R. Shen, J. Liu, F.Y. Hu, S. Liu, N. Cao, Y. Sui, Q.D. Zeng and Y.T. Shen, *CrystEngComm*., 2014, **16**,3387.

[29] S. K. Meher and G. R. Rao, *ACS Catal*., 2012, **2**, 2795.

[30] R.F.B. De Souza , A.E.A. Flausino , D.C. Rascio , R.T.S. Oliveira, E. Teixeira Neto, M.L. Calegaro, M.C. Santos, *Applied Catalysis B: Environmental*., 2009, **91**, 516.

[31] X. J. Liu, C. H. Cui, M. Gong, H. H. Li, Y. Xue, F.J. Fan and S. H. Yu, *Chem. Commun*., 2013, **49**, 8704.

[32]J. J. Lv, J. N. Zheng, S.S. Li, L. L. Chen, A. J. Wang and J.J. Feng, *J. Mater. Chem. A*., 2014, **2**, 4384.

Table of Contents

Catalyzed reduction of 4-nitrophenol with $NaBH_4$ and oxidation of methanol in acid solution, the Fe_3O_4@CeO_2/M (M=Pt and Pd) dual-heterostructural catalysts manifest superior catalytic efficiency and electrocatalytic reactivity and reusability.